CrossMark

RESEARCH ARTICLE

Direct Numerical Simulation of Turbulence Collapse and Rebirth in Stably Stratified Ekman Flow

S. M. Iman Gohari[1] · **Sutanu Sarkar**[1]

Abstract Direct numerical simulations of an Ekman layer are performed to study flow evolution during the response of an initially neutral boundary layer to stable stratification. The Obukhov length, L, is varied among cases by imposing a range of stable buoyancy fluxes at the surface to mimic ground cooling. The imposition of constant surface buoyancy flux , i.e. constant-flux stability, leads to a buoyancy difference between the ground and background that tends to increase with time, unlike the constant-temperature stability case where a constant surface temperature is imposed. The initial collapse of turbulence in the surface layer owing to surface cooling that occurs over a time scale proportional to L/u_*, where u_* is the friction velocity, is followed by turbulence recovery. The flow accelerates, and a "low-level jet" (LLJ) with inertial oscillations forms during the turbulence collapse. Turbulence statistics and budgets are examined to understand the recovery of turbulence. Vertical turbulence exchange, primarily by pressure transport, is found to initiate fluctuations in the surface layer and there is rebirth of turbulence through enhanced turbulence production as the LLJ shear increases. The turbulence recovery is not monotonic and exhibits temporal intermittency with several collapse/rebirth episodes. The boundary layer adjusts to an increase in the surface buoyancy flux by increased super-geostrophic velocity and surface stress such that the Obukhov length becomes similar among the cases and sufficiently large to allow fluctuations with sustained momentum and heat fluxes. The eventual state of fluctuations, achieved after about two inertial periods ($ft \approx 4\pi$), corresponds to global intermittency with turbulent patches in an otherwise quiescent background. Our simplified configuration is sufficient to identify turbulence collapse and rebirth, global and temporal intermittency, as well as formation of low-level jets, as in observations of the stratified atmospheric boundary layer.

✉ Sutanu Sarkar
   sarkar@ucsd.edu

   S. M. Iman Gohari
   sgohari@ucsd.edu

[1] Mechanical and Aerospace Engineering, University of California San Diego, 9500 Gilman Drive, La Jolla, USA

⚛ Springer

1 Introduction

The atmospheric boundary layer (ABL) is typically classified into three categories: neutral, convective and stable, based on the strength of stabilizing or destabilizing effects of buoyancy relative to wind shear. In the absence of the counteracting effects of humidity and advection, the ABL becomes stably stratified whenever the land/sea surface is cooler than the air above. Under these conditions, shear mostly generates turbulent motions, while negative buoyancy, which is a result of the radiative cooling, inhibits turbulence.

The stable ABL is further categorized into three regimes (Mahrt 1999; Sun et al. 2012). First, the weakly stable regime wherein temperature acts as a weakly active scalar and Monin–Obukhov similarity theory (MOST) (Obukhov 1971; Monin 1970) is applicable. Since buoyancy effects are weak, strengthening the stratification (temperature gradient) in the weakly stable regime results in an increase of turbulent heat flux. The second regime is characterized as moderately stable, where the turbulent heat flux is no longer increased by increasing stability because vertical velocity fluctuations and their correlation with temperature fluctuations decrease with the increased temperature gradient. Third, the strongly stable regime, where the ABL structure is different and one observes turbulence suppression and even collapse in the surface layer, internal gravity waves, and the decoupling of the surface from the outer region of the boundary. It is generally accepted that turbulence collapse is a complex process (Mahrt 1999) with *global intermittency*, when turbulent patches are interspersed in a quasi-laminar boundary layer, and *temporal intermittency*, manifesting as transient periods when the entire surface layer has relatively weak fluctuations. Several studies have implied that there are a number of external triggers which can result in globally intermittent flow, including non-turbulent wind oscillations, nocturnal low-level jets (LLJs), and solitary and internal gravity waves.

The stable boundary layer is dominant during nocturnal cycles, but there is still no comprehensive framework for its prediction. MOST describes the structure and scaling of different layers of the weakly stable ABL. Monin (1970) showed that this theory cannot properly reproduce the turbulent fluxes in the strongly stable regime. Data collected from atmospheric observations have not shown turbulence to be entirely suppressed under strongly stable conditions (Cuxart et al. 2000; Mauritsen and Svensson 2007). Also, quantitative understanding of strongly stable and globally intermittent turbulent flow from observations presents a challenge because of limitations in spatial and temporal coverage of observations and the difficulty of achieving accurate flux measurements under such conditions.

Large-eddy simulation (LES) is an efficient computational technique available for studying high Reynolds number turbulent flow and has been applied to the study of the stable ABL (Saiki et al. 2000; Kosović and Curry 2000; Beare et al. 2006; Zhou and Chow 2011). However, its ability to simulate strongly stable flows is uncertain. Prior studies suggest that LES may not accurately predict strongly stable flows (Basu and Porté-Agel 2006; Flores and Riley 2011; He and Basu 2015). It is widely shown in the literature that the flow statistics obtained from LES are strongly dependent on the utilized subgrid-scale (SGS) model, filter type, spatial resolution and other numerical techniques. When the energy-containing scales of motion are quite small and become of the same order as the grid size, as is the case in a strongly stable Ekman flow, LES may not properly provide correct subgrid fluxes of the turbulence (Jiménez and Cuxart 2005; Wiel et al. 2012).

To circumvent the limitations of observations and LES, a viable alternative is to perform direct numerical simulation (DNS), albeit at lower Reynolds numbers than in the ABL. This approach has become popular in the context of the stable ABL during the past few years (Flores and Riley 2011; Ansorge and Mellado 2014; He and Basu 2015). Stratified channel flow driven by a constant pressure gradient has been simulated, for both constant-temperature walls (Garg et al. 2000; Armenio and Sarkar 2002; Garcia-Villalba and Alamo 2011; He and Basu 2015) and a constant wall-cooling flux (Nieuwstadt 2005; Flores and Riley 2011). With increasing buoyancy, turbulence was found to be entirely suppressed in all of these studies. Armenio and Sarkar (2002) found collapse of turbulence at a critical value of $(h/L)_{cri} \approx 0.24$ in a case with $Re_* = u_* h/\nu = 180$, which differs from $(h/L)_{cri} \approx 0.51$ observed by Nieuwstadt (2005) at $Re_* = 360$, indicating a Reynolds number dependence for relaminarization. Here, L is the Obukhov stability length, h is the channel half-height, ν is the viscosity and $u_* = (\nu \partial_z U)^{0.5}$ is the friction velocity. More recently, Flores and Riley (2011) proposed a different controlling parameter, namely $L^+ = Lu_*/\nu$, with turbulence collapse for $L^+ \leq 100$. Here, u_* is a function of time and, during the transient evolution of stratified channel flow driven by a constant pressure gradient $d_x P$, it differs from the steady-state value of $u_\tau = (h d_x P/\rho)^{0.5}$. Moreover, Nieuwstadt (2005) found no global intermittency at moderate Reynolds numbers, whereas more recent studies have found global intermittency in channel-flow simulations (Garcia-Villalba and Alamo 2011; Flores and Riley 2011). Katul et al. (2014) have recently examined laboratory, field and DNS datasets, and find Reynolds number effects on relaminarization as well as in the dependence of flux Richardson number on gradient Richardson number.

Stratified open channel flow has been commonly used as a substitute for the stratified Ekman layer due to the similarities in the "near-wall region". However, Jiménez et al. (2009) found that the outer flow of boundary layers and channel flows are intrinsically different even in a non-rotating frame. Hence, Ekman flow is likely to be more suitable than open channel flow for including stratified ABL features. The Ekman boundary-layer thickness is determined by a balance between turbulent transport of momentum and the Coriolis term arising from the Earth's rotation and is proportional to $\delta = u_*/f$, where f is the Coriolis parameter. Coleman et al. (1992) and Ansorge and Mellado (2014) performed DNS of a stratified Ekman flow with an isothermal surface. Coleman et al. (1992) considered $Re_* = u_* \delta/\nu \approx 250$ and reported flow relaminarization when $(\delta/L)_{cri} > 0.14$. Ansorge and Mellado (2014) considered $Re_* = u_* \delta/\nu$ up to 1399, and found global intermittency and transient relaminarization at higher Re_* but, unlike the channel-flow studies, turbulence recovered after relaminarization with a monotonic increase, even for strong stratification.

We augment the existing understanding of stably stratified flows relevant to the ABL using a new DNS study where a stable buoyancy flux is imposed at the surface. We refer to this implementation of the stable boundary layer as " constant-flux stability" and note that the buoyancy difference across the boundary layer evolves dynamically (and the bulk Richardson number is unsteady) rather than being held fixed as in the case of constant surface temperature. This problem has not been investigated in previous DNS of stably stratified Ekman flow. The surface buoyancy flux is imposed on a neutral, turbulent Ekman layer and its value is varied among cases. Each case is simulated for five inertial periods to assess long-term behaviour. The objectives are as follows:

1. *Constant-flux stability*: what are the different regimes of stable stratification encountered during flow evolution? Is there a quasi-steady state with a well-defined boundary-layer structure?

2. *Turbulence collapse and recovery*: does this configuration show turbulence collapse, and global and/or temporal intermittency? What leads to turbulence recovery?
3. *Low-level jet (LLJ)*: does a LLJ form? How is the LLJ linked to turbulence properties?
4. *Comparison with other configurations*: what are the differences in the evolution with respect to channel flow and constant-temperature difference across Ekman flow? Are there similarities with observations of the stable ABL?

2 Formulation

The following equations for the conservation of momentum (under the Boussinesq approximation) and temperature are numerically solved,

$$\frac{\partial u_i}{\partial t} + \frac{\partial (u_i u_j)}{\partial x_j} = -\frac{\partial p}{\partial x_i} + \nu \nabla^2 u_i + \delta_{i3} \alpha g \theta + f \epsilon_{ij3}(u_j - U_\infty \delta_{j1}), \tag{1}$$

$$\frac{\partial \theta}{\partial t} + \frac{\partial (\theta u_j)}{\partial x_j} = \lambda \nabla^2 \theta. \tag{2}$$

Here, t is time, x_j is the spatial coordinate, u_j is the velocity, p is the pressure deviation from the the mean pressure field imposed by geostrophic forcing and the mean hydrostatic balance, ν is molecular viscosity, λ is thermal diffusivity, δ_{i3} is the Kronecker delta, ϵ_{ij} is the alternating unit symbol, g is the acceleration due to gravity, f is the Coriolis parameter, U_∞ is the geostrophic wind speed, α is the thermal expansion coefficient for air, and θ is the deviation of potential temperature from its constant reference value. The pressure, p, is computed by solving the Poisson equation that results from taking the divergence of the momentum equation and imposing zero velocity divergence at each timestep. In the region far above the surface, the flow is in geostrophic balance: the Coriolis force exerted on the geostrophic flow balances the large-scale pressure gradient force. Herein, the geostrophic wind direction is referred to as streamwise (x) while the direction of large-scale pressure gradient is referred as spanwise (y) and $z = x_3$ is the vertical direction. Horizontal boundary conditions are periodic. No-slip ($u = v = 0$) and impermeability ($w = 0$) are imposed at the smooth bottom. The top of the domain is taken to be stress-free ($\partial u/\partial z = \partial v/\partial z = 0$), impermeable, and adiabatic ($\partial \theta/\partial z = 0$) with a Rayleigh damping layer to minimize spurious reflection of gravity waves. Since the system is statistically homogeneous in horizontal directions, the Reynolds average of any quantity, e.g. $\langle u \rangle(z, t)$, is computed by averaging over horizontal planes.

A set of dimensional parameters $\{U_\infty, f, \nu, \lambda\}$ governs the dynamics of a neutrally-stratified Ekman flow over a smooth surface when turbulence has fully developed and sufficiently decorrelated from its initial condition (Coleman et al. 1992; Marlatt et al. 2010). This set of dimensional parameters results in two non-dimensional parameters: Reynolds number, $Re_D = U_\infty D/\nu$, and Prandtl number, $Pr = \nu/\lambda$, where $D = \sqrt{2\nu/f}$ is the laminar Ekman-layer depth (Spalart et al. 2008). By fixing $Pr = 1$, the Reynolds number is the only parameter that controls the steady-state solution of this flow regime. The laminar Ekman-layer depth is not a suitable length scale to describe momentum transport by turbulence. Hence, Re_D is not typically used as the governing parameter for turbulent Ekman flow; however, it provides a universal comparison point among different Ekman-flow studies. Instead, the turbulent regime is characterized by the surface friction velocity (u_*) and the boundary-layer length scale (u_*/f) leading to the friction Reynolds number, Re_*, as follows,

$$u_*^2 = \nu \frac{\partial \sqrt{u^2 + v^2}}{\partial z}\bigg|_{z=0}, \quad \delta = \frac{u_*}{f}, \quad Re_* = \frac{u_* \delta}{\nu} = \frac{u_*^2}{f\nu}.$$

In contrast to channel-flow simulations, u_* is not known prior to simulation in Ekman-layer studies and has a weak dependence on Re (Coleman et al. 1992).

Different velocity and length scales are used to describe near-surface and outer-layer behaviours of the flow. For the near-surface region, wall units, ν/u_*, and friction velocity, u_*, are chosen to normalize the statistics (denoted by superscript $+$), while outer-layer quantities are normalized by boundary-layer height, δ, and friction velocity, u_* (denoted by superscript $-$). The friction velocity and boundary-layer height used for non-dimensionalization of stratified cases are obtained from the neutral case, u_{*N} and $\delta_N = u_{*N}/f$, which do not change among the stratified cases. Finally, $1/f$ is chosen as the reference time scale.

2.1 Imposing Stratification and Constant-Flux Stability

After sunset overland in clear-sky conditions the atmosphere becomes stably stratified due to surface radiative cooling. A constant cooling flux, q_0, is applied at the surface to represent the effect of radiative cooling by fixing the potential temperature gradient, $\partial_z\theta$, at the surface so that $q_0 = -\lambda\partial_z\theta|_{z=0}$. Thus, the surface buoyancy flux defined as $B_0 = \alpha g q_0$ has a fixed nominal value during the evolution of the flow, and we refer to this type of stability as constant-flux stability. Different cases have different values of B_0. The time evolution of the stratification will be discussed in Sect. 5.

Various non-dimensional parameters are available to characterize the strength of buoyancy effects. Bulk Richardson number, Ri_b, is a possible measure of buoyancy effects and is defined as

$$Ri_b = \alpha g \delta_N \frac{\theta_\infty - \theta_s}{U_\infty^2},\tag{3}$$

where $\delta_N = u_{*N}/f$ and u_{*N} are obtained from the neutral Ekman layer and do not vary among cases.

In the present case of constant-flux stability, the surface potential temperature, θ_s, is a time-dependent variable computed using q_0 and the potential temperature at the first grid point above the surface. Therefore the buoyancy difference across the boundary layer changes with time. Consequently, the bulk Richardson number, Ri_b, is also a time-dependent quantity and varies substantially during the evolution of the flow. In contrast, when stratification is characterized by a constant temperature difference between the isothermal surface and the far field, the value of Ri_b, remains constant as the flow evolves. Constant-temperature stability has been used in prior DNS studies, e.g., Garcia-Villalba and Alamo (2011), Ansorge and Mellado (2014), Shah and Bou-Zeid (2014), Deusebio et al. (2014) and He and Basu (2015).

The more appropriate measure of stability for the present case with fixed surface buoyancy flux is the Obukhov length (Obukhov 1971), L, defined as,

$$L = -\frac{u_*^3}{\kappa B_0},\tag{4}$$

where κ is the von Kármán constant. Using wall units ν/u_*, the Obukhov length can be normalized as,

$$L^+ = \frac{Lu_*}{\nu} = -\frac{u_*}{\nu}\frac{u_*^3}{\kappa\alpha g q_0} = \frac{u_*^4}{\kappa\nu^2\alpha g \partial_z\theta|_{z=0}},\tag{5}$$

and, using outer-layer scaling, the normalized Obukhov length becomes

$$L^- = \frac{L}{\delta_N}.\tag{6}$$

For a region near the surface, this non-dimensional length scale can also be interpreted in terms of the gradient Richardson number at the surface,

$$Ri_{g,s} = \frac{N^2}{S^2} = \frac{\alpha g \partial_z \theta|_{z=0}}{u_*^4/v^2} = (\kappa L^+)^{-1}, \tag{7}$$

where the condition of $Pr = 1$ has been used. Therefore, L^+ contains stratification information and the stability condition near the surface region. A larger L^+ corresponds to a smaller $Ri_{g,s}$, suggesting a greater propensity for near-surface turbulence to persist despite surface cooling. Note that, since u_* is a strong function of time in stratified cases, so are L, L^+ and L^-.

A neutral Ekman boundary layer with constant temperature was allowed to evolve for $ft \approx 6$ to reach a quasi-steady state condition. Afterwards, a cooling buoyancy flux was applied at the surface with a value ramped up from zero to the nominal value, B_0, over $ft \approx 0.5$.

3 Numerical Method and Model Set-up

The algorithm utilized for numerically solving Eq. 2 is a modified version of that developed by Gayen and Sarkar (2011) and Jalali et al. (2014). The major features of the algorithm are as follows: (i) derivatives in the span-wise direction are computed using Fourier transforms, while the derivatives in the other two directions are approximated using the central second-order finite difference method; (ii) dealiasing of non-linear terms is performed using the 3/2 rule; and (iii) a low storage, third-order Runge–Kutta method is used for time advancement.

Table 1 lists the parameters of the simulated cases. It is worth noting that the actual boundary-layer thickness in the neutral case is $\approx 0.5 u_*/f = 0.5\delta_N$ leading to a friction Reynolds number based on actual boundary-layer thickness of $1121/2 = 561$. The computational domain is $L_x \times L_y \times L_z = (2\delta_N)^3 = (44D)^3$. An important requirement in DNS is proper resolution of viscous effects in the near-surface region that can extend up to $z^+ = 10$. Placing about 11 points in that layer in the neutral simulation yields a non-dimensional vertical grid spacing, $\Delta z^+_{min} < 1$. The grid is stretched moving upwards, but the grid spacing does not exceed $\Delta z^+ = 15$ at the top boundary. The streamwise resolution is $\Delta x^+ = 9.88$ and the spanwise resolution is $\Delta y^+ = 4.96$, similar to previous DNS of wall-bounded turbulent flows. Moreover, the adequacy of horizontal resolution has been ensured by checking global field planes and time-averaged spectra of the streamwise velocity component. Boundary conditions are no-slip and impermeability at the bottom, while stress-free and adiabatic

Table 1 Parameters of the DNS cases

Cases	N_s^2/f^2	L^-	$L^-_{x(y)}, L^-_z$	$\Delta x^+, \Delta y^+, \Delta z^+_{min}$	$N_x \times N_y \times N_z$
$N877$[a]	0	∞	2, 2	9.88, 4.96, 0.97	$193 \times 384 \times 193$
$SLD2$	1150	2	2, 2	9.88, 4.96, 0.97	$193 \times 384 \times 193$
$SLD1$	2300	1	2, 2	9.88, 4.96, 0.97	$193 \times 384 \times 193$
$SLD0.5$	4600	0.5	2, 2	9.88, 4.96, 0.97	$193 \times 384 \times 193$

[a] This case corresponds to a neurally-stratified Ekman layer flow with $Re_D = 877$ and $Re_* = 1121$. The values of L^- (non-dimensional Obukhov length) are based on u_{*N} obtained from $N877$ case. $L^-_{x(y)}$ and L^-_z are non-dimensional domain sizes

conditions are imposed at the top. A Rayleigh damping layer of 12 points is used at the top to minimize spurious reflection of gravity waves.

The horizontal domain needs to be sufficiently large to capture the largest dynamically important turbulent scales. The domain size used in the present study is similar to that used in Shah and Bou-Zeid (2014). Similar to their findings, this domain size is determined as sufficient to capture the dynamically-active turbulence scales in the neutral case. In the stratified cases, the final boundary-layer height, δ_{final}, is drastically decreased and it occupies about one-fourth of the computational domain height. The use of this shallower boundary layer for normalizing the domain size yields $L_{x(y)}/\delta_{\text{final}} = L_z/\delta_{\text{final}} \approx 4.45$, which are larger than those in the $N877$ case. Moreover, the integral length scales of horizontal velocities are found to be small compared to the periodic domain length, indicating the sufficiency of the domain size to capture the turbulence scales.

3.1 Model Set-Up

A series of direct simulations was performed as listed in Table 1. The effects of constant-flux stability on turbulent Ekman layer flow are studied for a fixed value of initial Reynolds number. The following parameters are also kept constant in each simulation: the Coriolis parameter, f, the Prandtl number, $Pr = 1$, and the air thermal expansion coefficient, α.

The normalized Obukhov length is used to quantify stabilizing buoyancy effects induced by the imposed surface buoyancy flux. Three different stratification levels are considered: $L/\delta_N \approx 2$ (weak), $L/\delta_N \approx 1$ (moderate) and $L/\delta_N \approx 0.5$ (strong). Since

$$L^+ = \frac{Lu_*}{\nu} = \frac{L}{\delta_N} \frac{u_*\delta_N}{\nu} = \frac{L}{\delta_N} Re_*, \tag{8}$$

the initial L^+ varies between 560 and 2242 among the cases. Substituting these values in the relation between L^+ and $Ri_{g,s}$ results in a gradient Richardson number of $O(10^{-3})$ near the surface. In the present model set-up, the flux Richardson number is $Ri_f \approx O(10^{-2})$, implying that, although the flow is exposed to constant-flux stability, the layer near the surface could still be turbulent.

4 Ekman Layer Under Neutral Conditions

We first consider the neutral Ekman boundary layer. The Reynolds number, $Re_D = 877$ (equivalently $Re_* = 1121$), is chosen to be sufficiently large to distinguish between the inner and outer layers. Ansorge and Mellado (2014) found large-scale structures originating from the outer layer and small-scale hairpin vortices stemming from the buffer layer at this value of Reynolds number. The neutrally stratified Ekman flow is used as the initial condition for the stratified simulations, and the coupling of these structures with buoyancy will be discussed in Sect. 5.

The wind speed decreases as the surface is approached, the Coriolis force directed rightward with respect to the wind direction decreases, and the resulting imbalance with the imposed large-scale pressure gradient force (leftward with respect to the geostrophic wind direction), causes the flow to veer to the left (counter-clockwise looking down from the top). The veering angle (β) of the surface stress with respect to the geostrophic wind, and the friction velocity are compared with Coleman et al. (1990), who found $U_\infty/u_{*N} = 18.22$ and $\beta = 19.55°$ for $Re_* = 1121$. There is good agreement between these values and those in
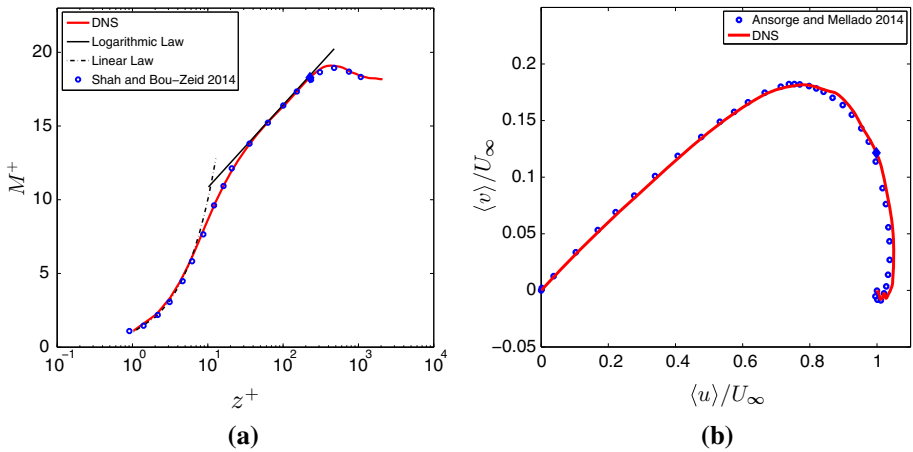
Fig. 1 Mean velocity in the neutral Ekman layer, N877 case. **a** Mean velocity profile compared with the result of Shah and Bou-Zeid (2014) and the logarithmic law: $M^+ = (1/\kappa) \ln(z^+) + B$, where $M = \sqrt{\langle u \rangle^2 + \langle v \rangle^2}$ is the mean horizontal velocity magnitude, $\kappa = 0.541$ and $B = 5.2$. The level $z^- = z/\delta_N = 0.21$ is marked with a *filled diamond symbol* in the velocity profile. **b** Velocity hodograph compared with the results of Ansorge and Mellado (2014)

the present DNS: $U_\infty/u_{*N} = 18.18$ and $\beta = 19.52°$ [the best fit for data is obtained with $A = 5.2$, $B = 0.1$ and $C_5 = -60$, following the nomenclature of Coleman et al. (1990)].

Figure 1 compares the mean velocity in the neutrally stratified case with the result of Shah and Bou-Zeid (2014) and the logarithmic law obtained from $M^+ = (1/\kappa) \ln(z^+) + B$, where $M = \sqrt{\langle u \rangle^2 + \langle v \rangle^2}$ is the mean horizontal velocity magnitude and $B = 5.2$. The logarithmic law is clearly observed in the simulation. The velocity profile departs from the logarithmic law at heights above which the flow starts to turn toward the geostrophic wind direction (see the marker at $z^- = 0.21$ in Fig. 1), in agreement with Tennekes (1973), Ansorge and Mellado (2014) and Shah and Bou-Zeid (2014). The velocity hodograph shown in Fig. 1b shows good agreement with the numerical study of Ansorge and Mellado (2014). Shah and Bou-Zeid (2014) computed the value of the von Kármán constant, κ, for Ekman flow using

$$\frac{\kappa z}{u_*} \left[\left(\frac{\partial \langle u \rangle}{\partial z} \right)^2 + \left(\frac{\partial \langle v \rangle}{\partial z} \right)^2 \right]^{1/2} = 1, \qquad (9)$$

finding that the exact value of κ is not precisely known, and it is not clear that its value is constant over the logarithmic region. Computation of $\kappa(z^+)$ in the present study shows that it varies with height ranging from 0.378 to 0.423, similar to previous atmospheric experiments and DNS studies (Spalart et al. 2008, 2009; Shah and Bou-Zeid 2014). The commonly cited value of 0.41 is used for κ in the logarithmic law shown in the plots.

We now turn to statistics of the fluctuations. Figure 2a compares the Reynolds stresses, plotted using inner-layer scaling, in the neutral Ekman layer with those for DNS of channel flow at $Re_* = 395$ (Moser et al. 1999). The near-wall region ($z^+ < 50$) contains the most vigorous turbulent activity. This plot depicts similarity between the inner layers of Ekman-layer flow and channel flow as demonstrated by Ansorge and Mellado (2014). Turbulent kinetic energy (TKE) budget terms are also found to be similar to those of channel flow in the inner layer as confirmed by Fig. 2b. Different line colours denote the various terms in the budget equation,
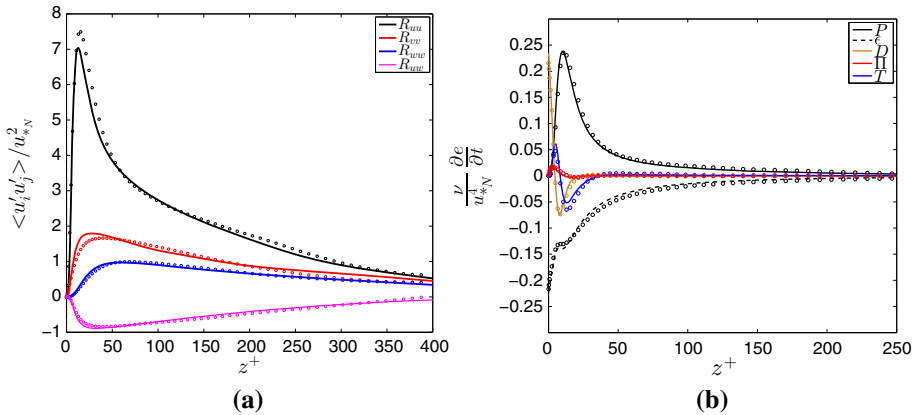
Fig. 2 Turbulence statistics. Results from the neutral Ekman layer, N877 case, is shown with *lines*. *Circles* show data from DNS of channel flow at $Re_* = 395$ (Moser et al. 1999). **a** Profiles of all the Reynolds stresses in channel flow normalized by the square of the friction velocity against normalized height ($z^+ = zu_{*N}/\nu$); **b** profiles of TKE budget terms normalized by u_{*N}^4/ν

$$\partial e/\partial t + \langle u \rangle_j (\partial e/\partial x_j) = \Pi + T + P + D - \epsilon, \qquad (10)$$

where the TKE $e = \frac{1}{2}\langle u_i' u_i' \rangle$, pressure transport rate $\Pi = -\partial \langle u_i' p' \rangle/\partial x_i$, turbulent transport $T = -\frac{1}{2}\partial \langle u_i' u_i' u_j' \rangle/\partial x_j$, shear production rate $P = -\langle u_i' u_j' \rangle(\partial \langle u_i \rangle/\partial x_j)$, viscous diffusion rate $D = \nu \partial^2 e/\partial x_j^2$, and viscous dissipation rate $\epsilon = \nu \langle (\partial u_i'/\partial x_j)(\partial u_i'/\partial x_j) \rangle$. TKE production and the loss by viscous diffusion peak in the buffer layer around $z^+ = 12$. In the viscous sublayer ($z^+ < 5$), the TKE is provided by viscous diffusion from the buffer layer that then dissipates locally. Turbulent transport acts as a loss of TKE (in $8 < z^+ < 16$), a region with high production. Above $z^+ = 35$, the dominant balance in the TKE budget is between the dissipation and production rates. There are strong similarities between the inner layer of the Ekman-layer flow and the channel flow; however, there are some differences, owing to variations in Reynolds number and flow configuration.

5 Transient Development of Ekman Flow Under Stable Stratification

Constant-temperature stability occurs when the surface of the initially neutral boundary layer is cooled to a constant temperature so that the bulk Richardson number, Ri_b, across the boundary layer does not change with time. Ansorge and Mellado (2014) and Shah and Bou-Zeid (2014) showed that, in such cases of constant-temperature stability, there is an initial transient period ($ft \approx 3$), during which the friction velocity, and hence the momentum flux, are rapidly reduced, followed by a slower turbulence recovery. In the present situation, a neutrally stratified flow is exposed to instantaneous surface cooling leading to constant-flux stability where the buoyancy contrast increases with time, leading to a concomitant increase of Ri_b that dynamically influences the flow evolution. For the constant-flux stability, the flow behaviour is found to be significantly different from that found in the case of constant-temperature stability. In particular, the initial transient period lasts longer, a low-level jet and shallow inversion form, and turbulence recovers following a collapse; there are several episodes of turbulence collapse/recovery. Many of the features of the initial transient period

are similar to the evolution of a cooled nocturnal boundary layer after sunset with residual turbulence in the outer layer.

It is important to note that turbulence in the entire column does not adjust immediately to the changes at the surface, and also that both u_* and $\delta = u_*/f$ evolve in time. Hence, u_* and δ of neutrally-stratified Ekman flow are used as reference scales to normalize the stratified results, unless otherwise noted.

The evolution of bulk properties shown in Fig. 3 illustrates changes in stability and turbulence, which are especially significant in cases with stronger buoyancy flux, namely $SLD0.5$ and $SLD1$. Figure 3a shows the time evolution of the friction velocity, non-dimensionalized by geostrophic wind speed, U_∞. The weakly stable case, $SLD2$, shows a nearly constant friction velocity in time whereas cases with higher stratification show significant variation. In moderately ($SLD1$) and strongly stable ($SLD0.5$) cases, the friction velocity increases, with a higher rate of increase for stronger stratification. The increase in u_* is substantial, almost 60 % in case $SLD0.5$. As will be discussed later, an LLJ forms, leading to a super-geostrophic velocity near the surface and, consequently, enhanced drag.

Remarkably, turbulence in the moderately and strongly stratified cases exhibits collapse followed by rebirth. Figure 3d shows the time evolution of volume-integrated TKE per unit area,

$$E = \int e\mathrm{d}z = \frac{1}{2}\int_0^{L_z} \langle u_i' u_i'\rangle \mathrm{d}z, \tag{11}$$

normalized using u_{*_N} and δ_N. The normalized E initially decreases due to the imposed stratification with a steeper decay in the case with the stronger stratification. In case $SLD2$ with the weakest stratification, the normalized E is observed to decrease to half of its neutral reference value at $ft \approx 1$ as previously found by Shah and Bou-Zeid (2014). In this case, the normalized E monotonically decays while the high-shear region near the surface sustains continuous turbulence. In cases with stronger stratification, the TKE decreases to nearly zero, indicating turbulence collapse. This is followed by strong intermittent bursts of turbulence and another event of turbulence decay. It is only after about an inertial period of $ft = 2\pi$ that these strong transient modulations of TKE subside in case $SLD0.5$. These modulations continue throughout the time period shown for the case with intermediate cooling flux, $SLD1$. Interestingly, the case with the highest cooling flux, which had periods of very low turbulence during its early evolution, has the highest integrated TKE at a later time. The time scale for the turbulence collapse near the surface for both the $SLD0.5$ and $SLD1$ cases is found to be approximately $4L/u_*$. Flores and Riley (2011) and Shah and Bou-Zeid (2014) also reported that the collapse time scale for turbulence is proportional to L/u_*.

The time evolution of various stability measures Ri_b, L^-, and L^+ is shown in Fig. 3b and c, with none of these quantities remaining constant in time. The bulk Richardson number, $Ri_b(t)$, defined in Eq. 3, increases with time primarily because the surface temperature, θ_s, decreases owing to the constant cooling flux at the surface. For the weakly stable case, the bulk Richardson number monotonically increases in time, while in the other two cases, $Ri_b(t)$ generally (not monotonically) follows an increasing trend because the surface temperature, θ_s, generally (not monotonically) decreases with time. Interestingly, there are occasions when $Ri_b(t)$ decreases over short time periods. As turbulence recovers, flow visualizations show bursting event periods when the Ekman layer progressively thickens. During these events of short duration, fluid with higher temperature at the top of the layer of turbulence is entrained into the surface layer, resulting in a short burst of surface temperature increase, i.e. reduction of $Ri_b(t)$. Normalized values of Obukhov length (Fig. 3c) change because of changes in $u_\star$ as can be deduced from Eqs. 5–6. The resultant increase in L^- is substantial in the cases
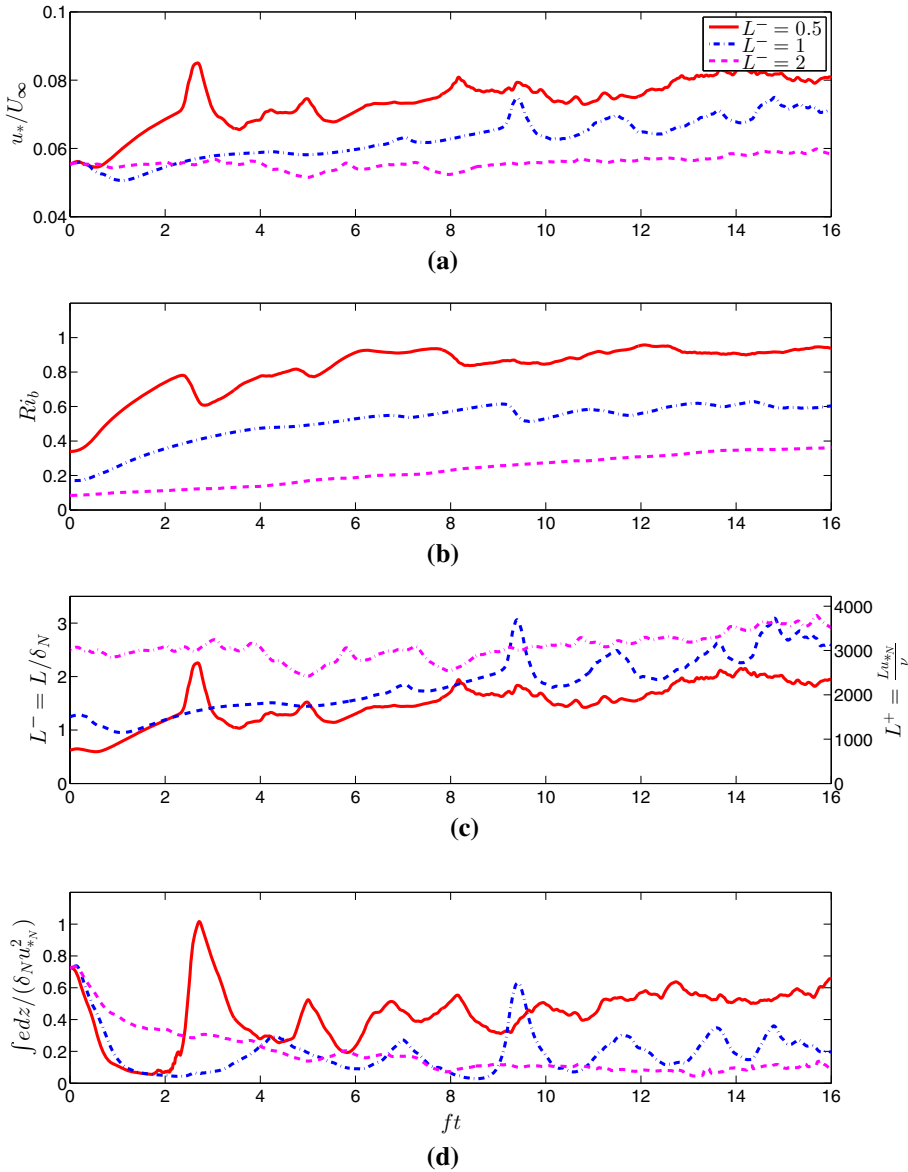
Fig. 3 The time evolution of: **a** normalized friction velocity (u_*/U_∞); **b** bulk Richardson number ($Ri_b = \alpha g \delta_N \frac{\theta_\infty - \theta_s}{U_\infty^2}$); **c** normalized Obukhov length ($L^- = L/\delta_N$, $L^+ = Lu_{*_N}/\nu$), and **d** integrated TKE ($\int e \mathrm{d}z/(\delta_N u_{*_N}^2)$). Surface cooling is imposed on a neutral Ekman layer at $ft = 0$

with higher stratification; e.g., in case $SLD1$, the increase is from a value of $L^- = 1$ to 2.5, close to the value of L^- at that time for the weakly stable case.

Figure 4 shows time series of fluctuating quantities at a point in the surface layer for case $SLD0.5$. The events comprising collapse/rebirth of turbulence that were shown in the plot of integrated TKE are also evident here. For instance, the temperature fluctuation (Fig. 4c)
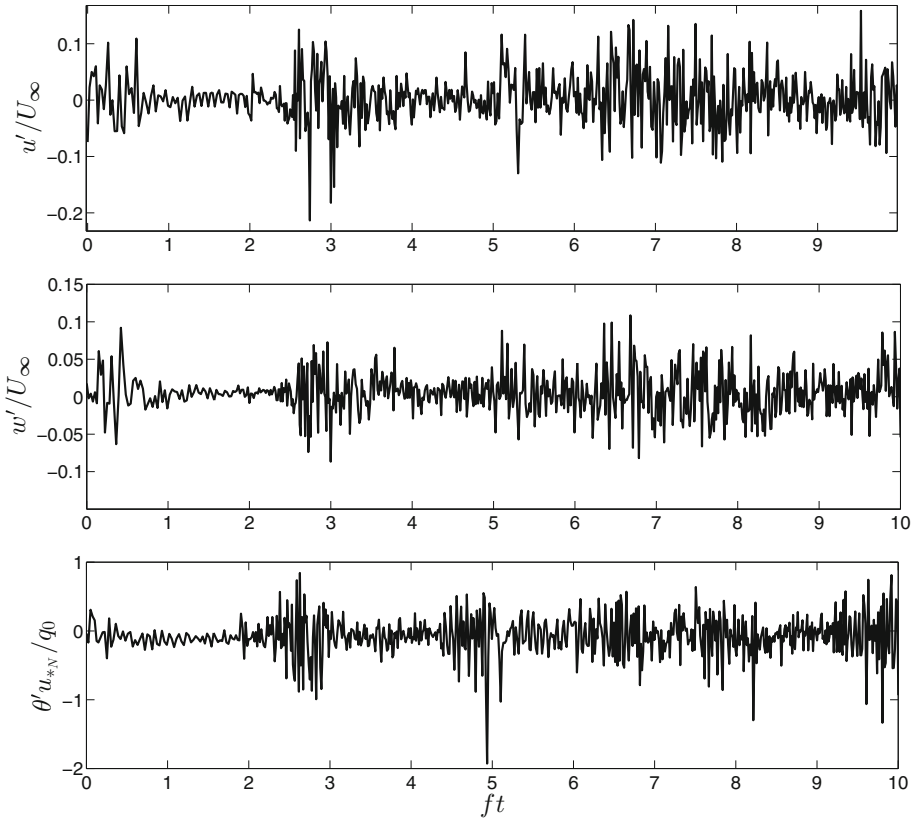
Fig. 4 The time evolution of instantaneous fluctuations at a height of $z^- = 0.185$ in the centre of horizontal domain for case *SLD*0.5: **a** streamwise velocity fluctuation (u'/U_∞); **b** vertical velocity fluctuation (w'/U_∞); **c** potential temperature fluctuation ($\theta' u_{*N}/q_0$)

shows clearly the two prominent turbulent bursts that span the intervals $ft = \{2.5, 3\}$ and $\{4.5, 5\}$. The initial collapse of turbulent velocity fluctuations occurs over a period of $ft = 1$ after the commencement of the surface cooling flux.

Figure 5 shows visualizations of normalized streamwise velocity fluctuation, u'/u_*, in near-wall horizontal planes at $z^+ = 15$ (left column) and in the outer layer at $z^- = 0.185$ (right column) to illustrate collapse and rebirth of turbulence in the strongly stratified case *SLD*0.5. The initial near-wall streaks (top left) present in neutrally stratified Ekman flow are nearly extinguished at $ft \approx 1.25$ (middle left) and reappear at $ft \approx 2.5$ (bottom left). The pattern at $ft \approx 2.5$ is suggestive of global intermittency as turbulent patches inclined in streak-like patterns are found in an otherwise quiescent flow. The plane in the outer layer (right column) also shows weakening of fluctuations at $ft \approx 1.25$ followed by patchy turbulence at $ft \approx 2.5$. Similar plots for the least stable case are shown in Fig. 6. In contrast to *SLD*0.5, continuous turbulence persists near the surface in the weakly cooled case *SLD*2. However, buoyancy effects are stronger in the outer layer; fluctuations are weaker at $ft \approx 2.5$ (bottom right) relative to the initial neutral state (top right).

The structure of the Ekman layer changes in the presence of strong stratification via the formation of an LLJ as has been observed in field studies (Cuxart et al. 2000; Banta 2008). Figure 7 shows plots of the mean profiles of u and v (both shown in the left panel), and
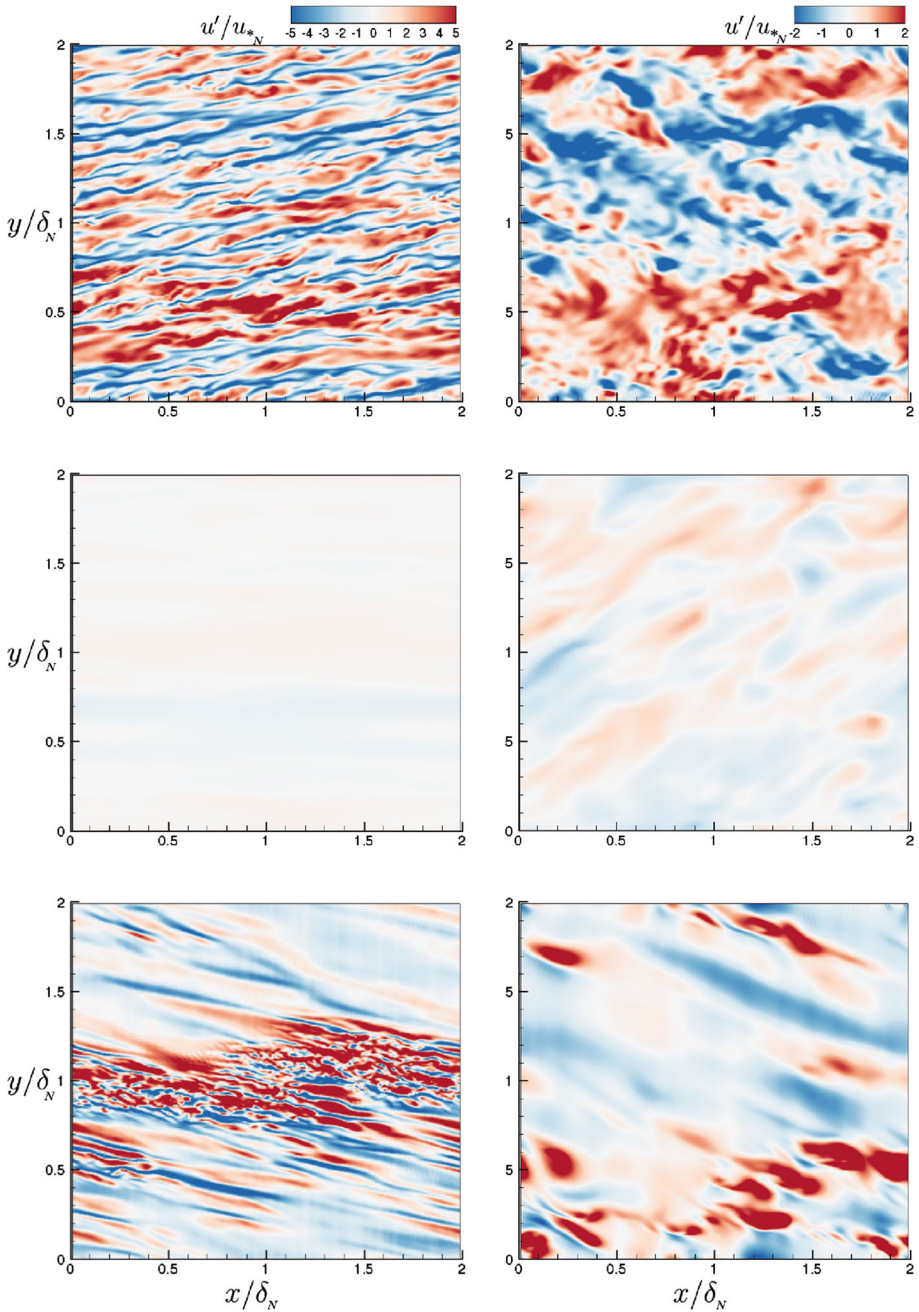
Fig. 5 Collapse and rebirth of turbulence in $SLD0.5$. Streamwise velocity fluctuation, u'/u_{*_N}, on horizontal planes at height $z^+ = 15$ (*left*) and $z^- = 0.185$ (*right*): $ft = 0$, neutral case (*top*); $ft \approx 1.25$ (*middle*); $ft \approx 2.5$ (*bottom*)
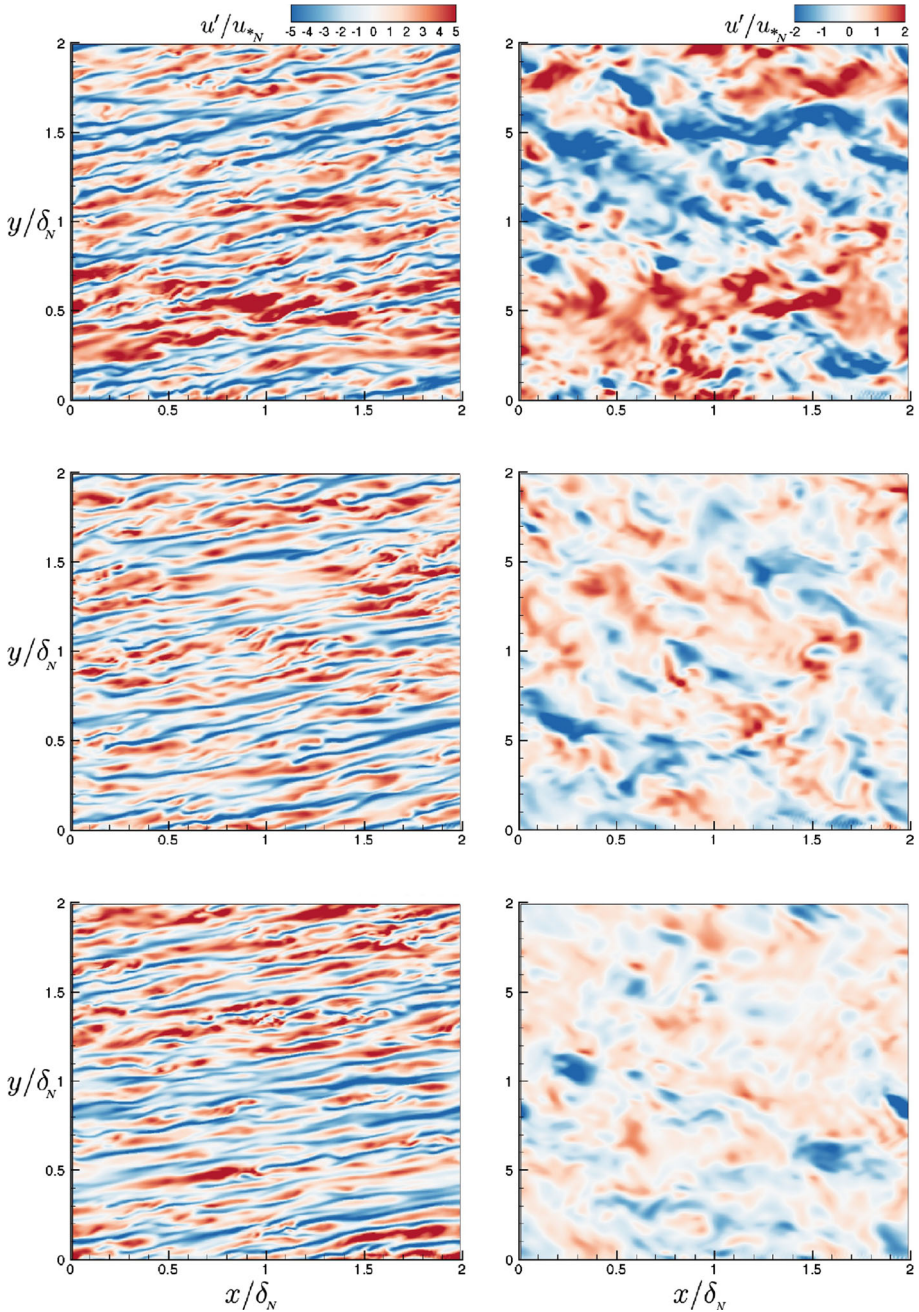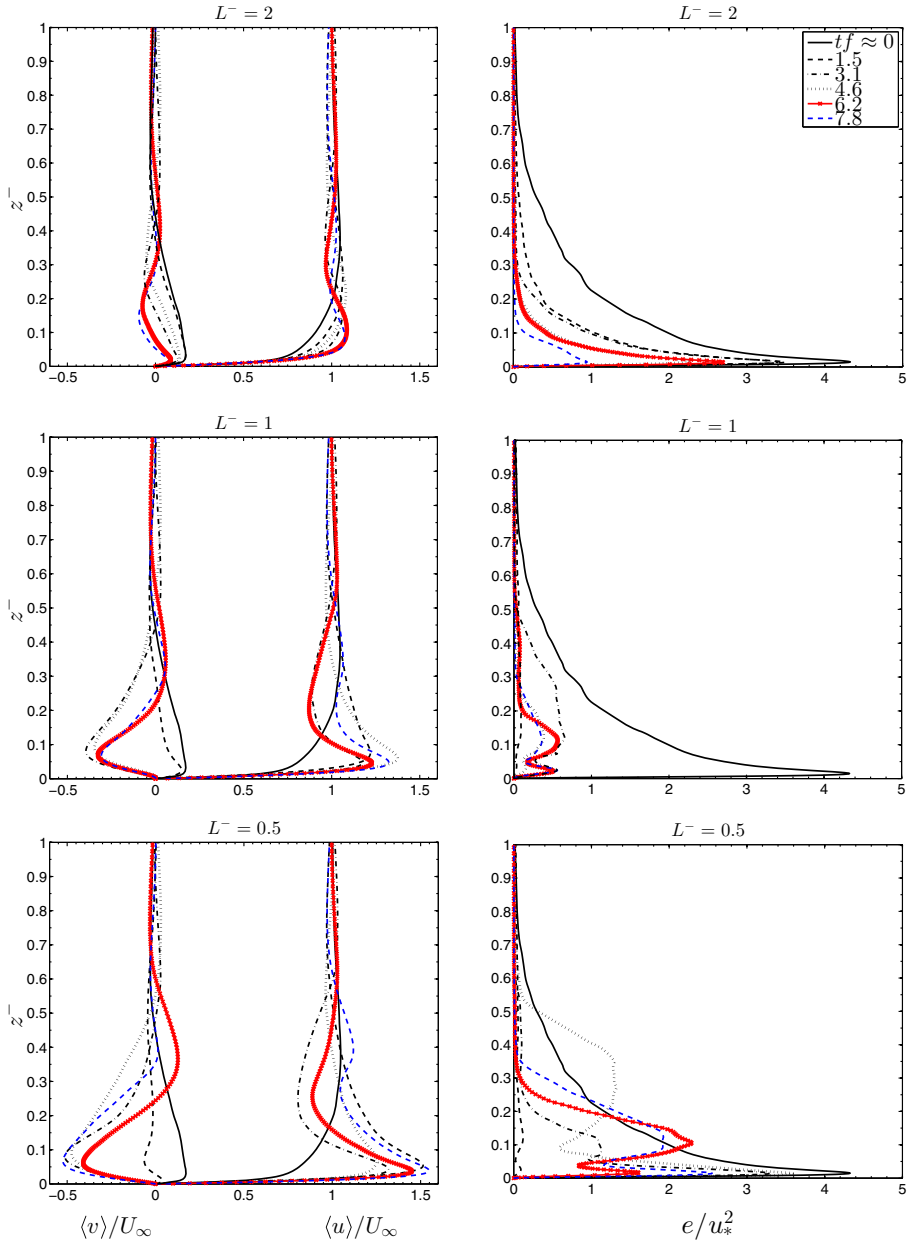
Fig. 6 Continuous turbulence in case *SLD*2. Streamwise velocity fluctuation, u'/u_{*_N}, on horizontal planes at height $z^+ = 15$ (*left*) and $z^- = 0.185$ (*right*): $ft = 0$, neutral case (*top*); $ft \approx 1.25$ (*middle*); $ft \approx 2.5$ (*bottom*)

Fig. 7 Profiles of normalized horizontal mean velocities (*left column*) and normalized TKE (*right column*) for weakly stable, *SLD*2 (*top row*), moderately stable, *SLD*1 (*middle row*), and strongly stable, *SLD*0.5 (*bottom row*) cases. Velocity profiles show increased wind speed and a LLJ

normalized TKE (right panel) at different times. For the least stable case (top row), the velocity profile up to $z^- = 0.6$ exhibits an inertial oscillation during the initial transient. The "spiral" of the classical Ekman solution (assuming constant viscosity and steady state) is more evident in the velocity profiles in case *SLD*2 relative to the neutral case. The velocity hodograph and
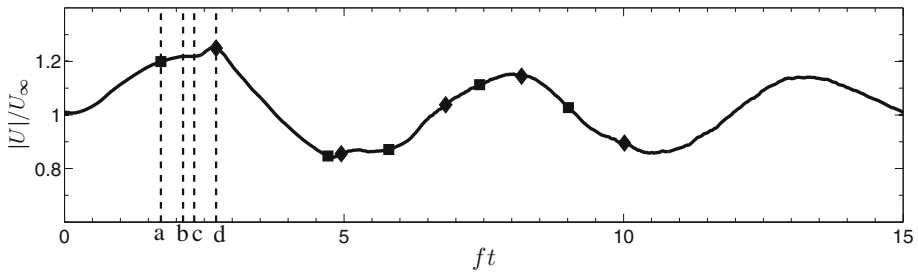
Fig. 8 The time evolution of velocity magnitude normalized by geostrophic wind speed ($\langle|u|\rangle/U_\infty$) at height $z^- = 0.185$. *Tick marks* (*a–d*) denote the different times corresponding to the *curves* show in each of the *panels* in Fig. 9. *Squares* indicate turbulence collapse and *diamonds* indicate turbulence rebirth

veering angle (not plotted) follow patterns similar to the neutral reference case. In the other two cases with a greater surface buoyancy flux, the transient period is characterized by rapid changes in the surface-layer wind speed and wall stress. In case *SLD*0.5, an LLJ forms with peak velocity at $z^- \approx 0.05$ and shear that extends up to $z^- = 0.4$ (bottom left of Fig. 7). The height of the velocity maximum is lower and the maximum overshoot from the geostrophic wind speed, $u/U_\infty - 1$, increases with increasing cooling flux. This maximum overshoot occurs at $ft \approx 2.5$, and is almost twice as large for *SLD*0.5 compared to *SLD*1. The LLJ qualitatively changes the inclination of the surface flow from counter-clockwise to clockwise with respect to the geostrophic flow. This preferred inclination of near-surface mean velocity is a result of the strong LLJ formation that emerges in Ekman flow under the present constant-flux stability implementation. The vertical distribution of TKE and its time evolution show how a neutrally stratified flow responds to constant-flux stability (right panel of Fig. 7). For the least stable case and in agreement with Fig. 6, these plots show that turbulence is extinguished or strongly suppressed in the outer layer while the surface layer is continuously turbulent albeit at a reduced level with respect to the neutral situation. However for case *SLD*0.5, turbulence is extinguished near the surface at $ft \approx 1.5$, but persists at a reduced level in the outer layer. This residual turbulence in the outer layer is a common feature of the nocturnal boundary layer (Stull 1988).

The time evolution of velocity magnitude, normalized by geostrophic wind speed ($\langle|u|\rangle/U_\infty$), and shown for $z^- = 0.185$ in Fig. 8, illustrates that the velocity exhibits super-geostrophic values during persistent inertial oscillations. Multiple occurrences of turbulence collapse (square symbols) and rebirth (diamond symbols) are also marked. As mentioned, strong stratification results in collapsed turbulence near the surface (Fig. 5) and LLJ formation (Fig. 7). As a result of the near-wall layer decoupling from the outer layer during times of turbulence collapse, the outer layer speeds up, inducing a local jet with strong shear. The high-shear region between the LLJ and the surface is dynamically unstable as explained in Sect. 3.1 and leads to strong turbulence production.

To better understand turbulence rebirth, profiles of several TKE budget terms, TKE, gradient Richardson number and mean velocity are plotted at different times between the end of a collapse ($ft = 1.7$) and well into rebirth ($ft = 2.7$) in Fig. 9. Transport of fluctuating energy from the outer layer into the surface layer combined with enhanced turbulence production from strengthening of LLJ shear leads to turbulence rebirth as elaborated below. Although the TKE, shown in Fig. 9d, is small at $ft = 1.7$ (solid line in the plots), it is larger in the outer layer relative to the surface layer. Among the budget terms, the pressure transport is the largest at $ft = 1.7$ and also earlier during the collapse. At $ft = 2.1$ (dotted line), the pressure

transport (Fig. 9a) is larger than the turbulence transport (Fig. 9c), and the shear production (Fig. 9b) increases to become comparable to the pressure transport. Figure 9b shows that shear production increases dramatically from nearly zero at $ft = 1.7$ to substantial values during TKE rebirth. The LLJ nose (point of maximum velocity) is at $z^- \approx 0.05$ where the mean shear is locally zero as is the shear production. The upper flank of the jet, above the nose, is broader than the lower flank and has non-zero shear production until $z^- = 0.3$ at $ft = 2.7$. The TKE at $ft = 2.7$ (Fig. 9d) has a double-lobed structure which extends all the way up to $z^- = 0.4$. The near-wall peak in TKE corresponds to the shear in the lower flank of the LLJ while the second peak is associated with the shear in the upper, broader flank of the LLJ. At $ft = 2.7$, there is significant turbulent transport (Fig. 9c) into the core of the jet, centred around $z^- = 0.05$ due to transport from both the lower and upper flanks of the jet.

Profiles of Ri_g, a measure of the competition between buoyancy stabilization and shear production, are shown in Fig. 9e. The region very near the surface is always shear dominant with nearly zero values of Ri_g, while the values of Ri_g in the outer layer are significantly larger. During the turbulence rebirth event, the peak speed of the LLJ increases until $ft = 2.3$ as shown in Fig. 9e. The peak shear increases and subsequently Ri_g decreases, reaching its minimum value of 0.225 at $ft \approx 2.1$. Having a subcritical ($Ri_g < 0.25$) region near the nose of the jet enhances the rejuvenation of surface-layer turbulence. Shortly afterwards, the residual outer layer recouples with the surface layer and the eventual boundary layer emerges. Due to the turbulent entrainment at the top of the LLJ, the layer of turbulence progressively thickens in time. The TKE at $ft = 2.7$ extends up to $z^- = 0.4$ as noted earlier. After recoupling of the inner and outer layers through turbulence, the peak velocity decreases at $ft = 2.7$ relative to $ft = 2.3$, but the outer layer (upper flank of the LLJ) maintains an elevated level of shear and associated shear production. Global intermittency (patches of small-scale turbulence) is found in both outer and surface layers after turbulence recovery. Notably, the structures in the velocity field of the two layers appear completely different, both from each other and from those seen in the neutral reference. The angle along which streamwise-velocity streaks are oriented in the surface layer is estimated to be around 20° (shown in bottom left panel of Fig. 5).

Collapse and rebirth of turbulence have been reported in previous atmospheric observations by Banta et al. (2007), who observed a two-layered structure under a strongly stable condition consisting of a shallow boundary layer close to the surface and an almost quiescent layer above. They found that the shear associated with the LLJ in the quiescent layer was initially isolated from the surface layer, but eventually LLJ-generated turbulence burst downward to the surface. They also reported turbulence rebirth after a 6-h period of turbulence collapse, which is equivalent to $ft \approx 2.4$ in non-dimensional form and therefore consistent with the results obtained in the present study.

6 The Stratified Ekman Layer at Long Time

In the previous section, we have shown that there are episodes of temporally collapsed turbulence as Ekman flow responds to moderate and strong levels of cooling flux. This collapse is followed by turbulence rebirth near the surface due to a combination of fluctuation transport from the outer layer to the inner layer and intensification of shear in the LLJ. Globally intermittent flow with streaks of patchy turbulence in an otherwise quiescent flow is found after rebirth. Two inertial periods later, a regime of continuous but globally intermittent turbulence is reached with velocity fluctuations on horizontal planes whose organization
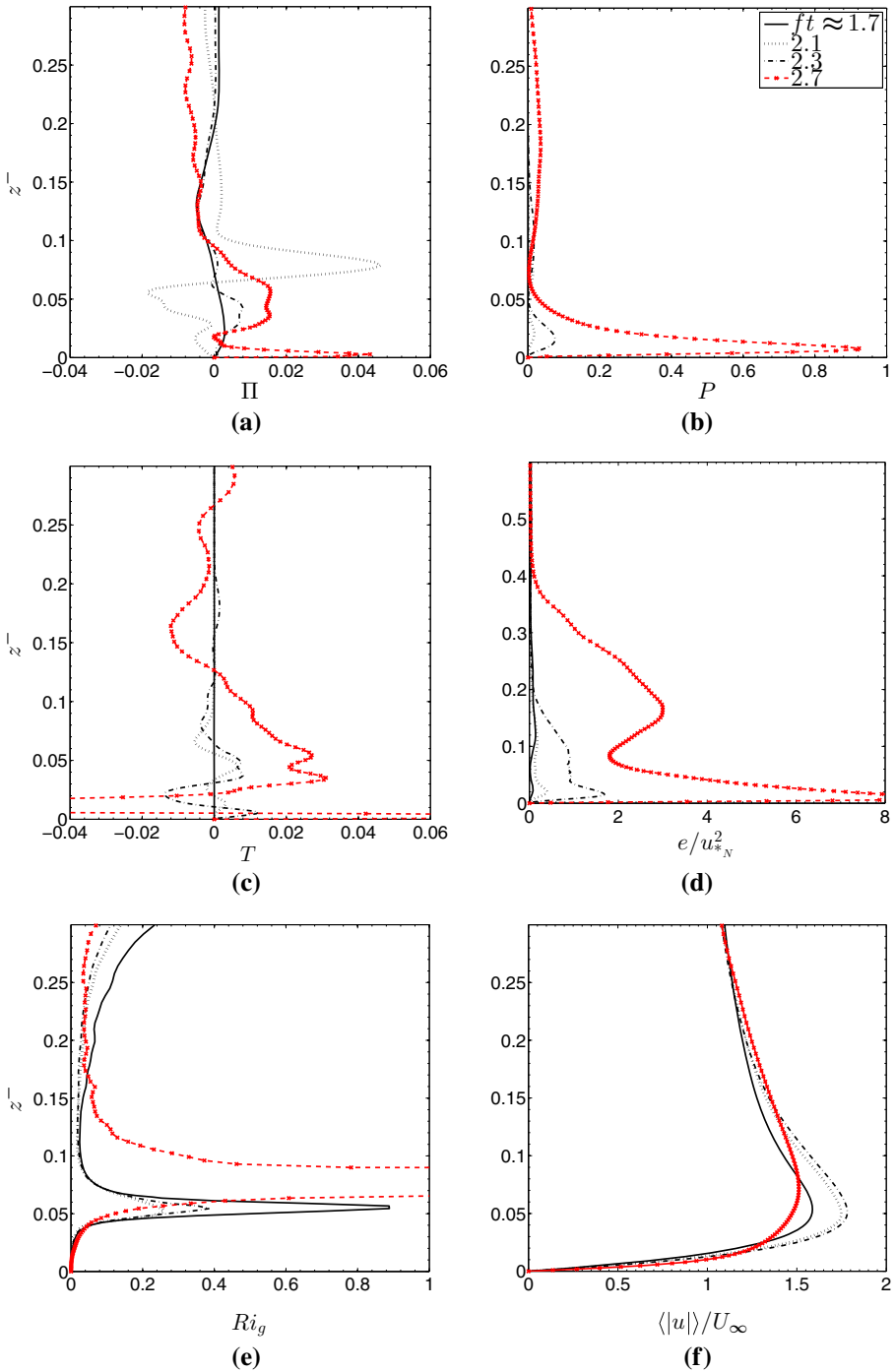
Fig. 9 Evolution during the turbulence rebirth event between $ft = 1.7$ and $ft = 2.7$ in case $SLD0.5$: **a** pressure transport; **b** shear production; **c** turbulent transport terms in the TKE budget equation normalized by u_{*N}^4/ν; **d** TKE (e/u_{*N}^2); **e** gradient Richardson number; **f** mean velocity magnitude ($\langle|u|\rangle/U_\infty$)
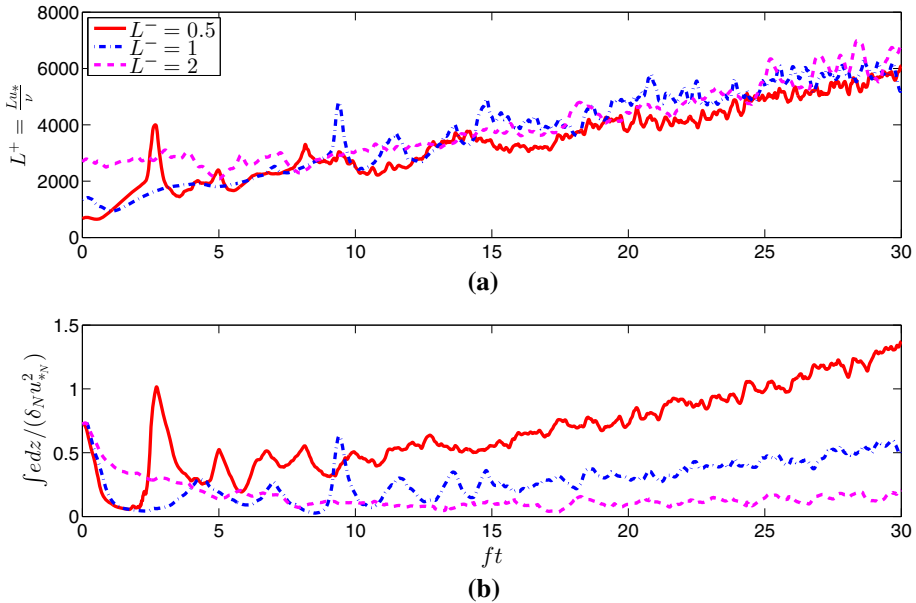
Fig. 10 The time evolution of: **a** normalized Obukhov length scale (L^+), and **b** volume-integrated TKE ($\int e\mathrm{d}z/(\delta_N u_{*N}^2)$)

does not change qualitatively in time. However, the flow is not quantitatively at statistical steady-state even after five inertial periods.

The normalized Obukhov length (L^+) and integrated TKE ($E/(u_{*N}^2 \delta_N)$) are compared for the stratified cases in Fig. 10. Although the initial values of L^+ are quite different among cases, they become comparable after about one inertial period. When the imposed surface buoyancy flux increases, the friction velocity increases due to a stronger LLJ, thus increasing L^+ to values comparable to the cases with weaker buoyancy flux imposed at surface. Thereafter, all cases evolve similarly, exhibiting a consistent increase of friction velocity and, therefore, Obukhov length with time. It is noted that the surface value, $Ri_{g,s}$, of gradient Richardson number is directly related to L^+, so the evolution of $Ri_{g,s}$ is also similar among the cases. Figure 10a shows large values of L^+ that continue to increase, consistent with the continuous turbulence found for Ekman flows with surface cooling flux. Figure 10b shows $E/(u_{*N}^2 \delta_N)$ for the stratified cases. It shows that, despite the initial collapse in case *SLD*0.5, the normalized E reaches and exceeds that of the neutrally stratified case as previously observed by Nieuwstadt (2005), Flores and Riley (2011) and Ansorge and Mellado (2014).

Profiles of several statistics are shown in Fig. 11 to illustrate the Ekman flow at long time ($ft \approx 30$). A comparison of the mean velocity profiles for the neutral reference and the stratified cases is shown in Fig. 11a. In all cases, constant-flux stability changes the mean velocity structure. As the stability increases, a stronger LLJ with lowered height of maximum in the velocity profile emerges. The stronger and lowered LLJ results in an increased mean velocity gradient near the surface and hence, the value of u_*/U_∞ is found to be largest in the case with the strongest rate of stratification. Similar behaviour is reported by Deusebio et al. (2014). The value of u_*/U_∞ is 0.091, 0.079 and 0.068 for the *SLD*0.5, *SLD*1 and *SLD*2 cases respectively, while the veering angle of the surface stress (clockwise with respect to the geostrophic wind direction) is 9.43°, 6.95° and 4.06°, respectively. It is important to
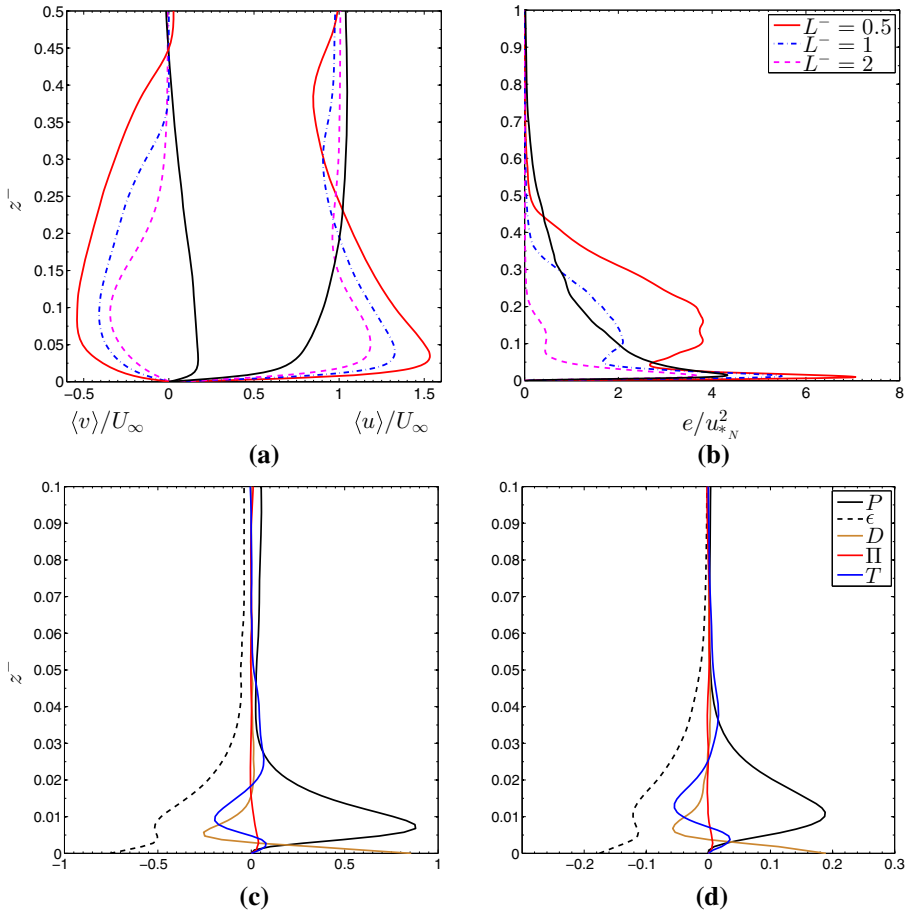
Fig. 11 Profiles of normalized statistics at long time ($ft \approx 30$) against normalized height: **a** velocity; **b** TKE. Here all three stratified cases are plotted as well as the neutral case shown in *solid-black*. **c** TKE budget terms normalized by $u_{*_N}^4/\nu$ for *SLD*0.5 case; **d** similar budget terms for *SLD*2 case. Terms that are not plotted have been computed and found to be negligibly small

note that in the stable Ekman layer, the height of the LLJ nose is a good indicator of the height of the surface turbulent layer, and is observed to decrease with increasing stability as shown in Fig. 11a. It is of further interest to compare the location of the LLJ in the DNS with that of ABL studies. Considering typical values of friction velocity $u_* \approx 0.3$ m s^{-1} and $f \approx 10^{-4}$ s^{-1}, results in $\delta_N = u_*/f \approx 3000$ m. The height of the LLJ nose deduced from the profiles of Fig. 11a, $0.05\delta_N = 150$ m, is within the typical range of LLJ heights in the ABL (Saiki et al. 2000; Kosović and Curry 2000; Beare et al. 2006; Zhou and Chow 2011). The height of the LLJ nose deduced from

The vertical distribution of TKE is shown in Fig. 11b. There is notably a two-layer structure with the minimum TKE at the LLJ nose height. The vertical distribution of cases *SLD*1 and *SLD*0.5 shows two local maxima, one below and the other above the LLJ nose level, the former located at a height of about one-fifth the LLJ nose height, and the latter located at approximately three times the height of nose. The Stable Atmospheric Boundary Layer Experiment in Spain-1998 (SABLES-98) data reported by Cuxart et al. (2000) showed the

formation of LLJ in the stably stratified nocturnal boundary layer. The Richardson number profiles exhibited low values above the LLJ peak velocity location suggestive of shear-induced mixing. Turbulence profiles taken later by Conangla and Cuxart (2006) showed local peaks of TKE and heat flux above the location of the LLJ peak velocity. The LES of Cuxart and Jiménez (2007) exhibited a two-layered structure of TKE, with minimum values at LLJ nose level and local maxima above and below the nose level. However, their LES was initialized with velocity and temperature profiles of an observed LLJ in contrast to the present DNS where the LLJ is *not* assumed but forms as a response of the neutral Ekman layer to stable surface buoyancy flux. Cuxart and Jiménez (2007) reported $e/u_*^2 \approx 6$ for the maximum below the LLJ nose and $e/u_*^2 \approx 3$ for the maximum above, consistent with the present results. Moreover, atmospheric observations (Smedman et al. 1993) of an LLJ over the Baltic Sea showed similar findings regarding these maxima locations and TKE values. The consistency of results obtained here with previous atmospheric studies demonstrates the appropriateness and relevance of the present simulations to atmospheric flows.

Figure 11c and d compare the TKE budget terms in cases with the strongest and weakest stability. The buoyancy flux term is not shown in these plots because it is relatively small in comparison to the other terms (less than 5 % of the maximum TKE production). This implies that the direct impact of constant-flux stability on the flow is not through buoyancy destruction, a finding that is similar to those in channel-flow studies with constant-temperature stability by Armenio and Sarkar (2002) and in Ekman layers by Ansorge and Mellado (2014) and Shah and Bou-Zeid (2014). Figure 11c indicates that there is a significant increase in shear production of TKE which is a result of the high-shear region between the surface and the LLJ nose (Fig. 11a). Correspondingly, the TKE (Fig. 11b) near the surface reaches and exceeds that of the neutrally stratified case. Furthermore, in the *SLD*0.5 case, the normalized TKE shear production in the region $0.1 < z^- < 0.2$ has an almost constant value of about 0.1, which is comparable to about half of the peak shear production in the neutral $N877$ case. Case *SLD*0.5 has a velocity profile (Fig. 11a) with a broad region of shear extending above $z^- = 0.4$, leading to higher shear production and therefore an upper lobe with significant TKE (Fig. 11b). The increased shear production at long time in the Ekman flow is the most dominant impact of constant-flux stability on the TKE budget. The TKE dissipation rate is also observed to increase in order to balance the TKE production rate. The dominant TKE terms near the surface are the dissipation rate and the viscous diffusion terms. Turbulent and pressure transport terms have smaller contributions in the TKE budget compared to the dominant terms, i.e. dissipation and production.

The structure of the temporally-evolving temperature field is of particular interest. In all cases, a new boundary layer is formed with a thermal inversion that is capped by a thermocline. Interestingly, case SLD2 with moderate surface buoyancy flux eventually exhibits a larger stable temperature gradient (dashed curve in Fig. 12a) in the boundary layer than the strongly cooled case SLD0.5. Though not immediately clear, this behaviour is consistent with the preceding discussion of a boundary layer with large TKE associated with LLJ shear in case SLD0.5. The two cases with larger stratification (SLD1 and SLD0.5) exhibit similar profiles of gradient Richardson number (Fig. 12c) when plotted against height normalized with the inversion height, $h_{N_{\max}}$. The critical value of $Ri_g = 0.25$ occurs at $z/h_{N_{\max}} \approx 1$. The root-mean-square of the temperature fluctuations (Fig. 12d) also tends to peak in the thermocline at the height of maximum temperature gradient.
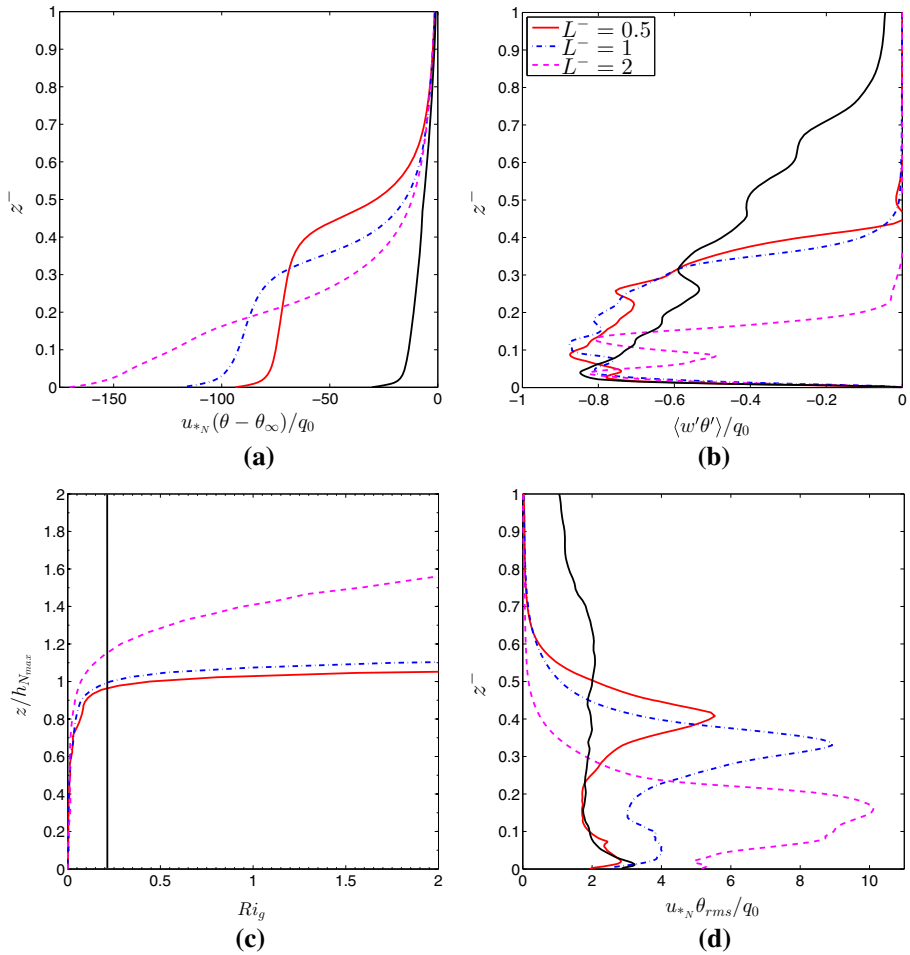
Fig. 12 The thermal structure of the boundary layer at large time ($ft \approx 30$): **a** potential temperature ($u_{*_N}(\theta - \theta_{\infty})/q_0$); **b** vertical buoyancy flux, ($\langle w'\theta' \rangle/q_0$); **c** gradient Richardson number (height has been normalized with height of maximum of N in this plot); **d** variance of temperature fluctuations ($u_{*_N}\theta_{rms}/q_0$). Here all three stratified cases are plotted as well as the neutral case shown in *black*

7 Summary and Conclusions

The response of a neutral Ekman layer to the stabilizing influence of buoyancy was studied using direct numerical simulation (DNS). A surface cooling flux was imposed leading to constant-flux stability characterized by a dynamically evolving (temporally increasing) net buoyancy difference across the flow. Three cases were simulated with different values of the initial Obukhov length: twice, equal and half the neutral boundary-layer length scale, u_*/f, corresponding to weak, moderate and strong stability, respectively.

Under strong stability, there is temporal intermittency (extinguishing of turbulence in the boundary layer followed by rebirth) as well as global intermittency (presence of turbulence patches inside an otherwise quiescent boundary layer) in the flow field during the initial transient that lasts about 1.5–2 inertial periods. The turbulent patches contain small-scale

structures that are organized into inclined streaks. The patches have a preferred negative (clockwise) inclination with respect to the direction of the geostrophic flow.

The present DNS shows that there are significant differences in turbulence characteristics and boundary-layer structure when a neutrally stratified Ekman layer is exposed to constant-flux stability (through imposed fixed surface cooling flux) rather than the previously-studied case of constant-temperature stability (fixed temperature imposed on surface). In the Appendix, we briefly compare the present DNS of constant-flux stability with simulations that have constant surface temperature. Constant-flux stability leads to the formation of a strong low-level jet (LLJ) with large super-geosotrophic velocity, the increase in surface stress relative to the neutral state, turbulence collapse/rebirth events followed by continuous but globally intermittent turbulence, the decrease in the surface-layer height (defined as the height of the maximum in the velocity profile), and a double-peaked profile of turbulent kinetic energy with the minimum at the LLJ nose.

The stratified cases exhibit an initial collapse of surface-layer turbulence with a timescale of L/u_* consistent with the DNS of Flores and Riley (2011) and Shah and Bou-Zeid (2014), and the observations of Banta et al. (2007). Furthermore, as the turbulence collapses, the near-surface flow accelerates to form an LLJ. Unlike non-rotating boundary-layer flows, the reduction in turbulent momentum flux by buoyancy leads to an imbalance between the Coriolis force and the imposed pressure gradient which generates the LLJ as well as inertial oscillations. Subsequently, turbulence is reborn, consistent with field observations of the nocturnal boundary layer, e.g. Banta et al. (2007). The time-height plots of TKE budget terms and gradient Richardson number suggest that transport of fluctuations from the outer layer to the surface layer, as well as the increased shear of the LLJ, result in the recovery of shear production at the wall and, thus, TKE in the surface layer. Additionally, the time series of volume-integrated TKE shows that turbulence recovery is not monotonic but occurs in collapse/rebirth cycles indicating temporal intermittency. After recovery, turbulence differs from the neutral state, exhibiting global intermittency with patches of small-scale turbulence embedded in quasi-laminar regions.

Results of stably stratified flows at long time (after about 1.5–2 inertial periods) show that there is continuous turbulence in all three cases. An inversion layer forms at shallower height to cap the boundary layer. When the value of the prescribed surface buoyancy flux is increased, the LLJ strengthens and the friction velocity increases so as to keep the Obukhov length comparable among cases even though the applied surface buoyancy flux varies by a factor of four among them. The evolution of the normalized Obukhov length, L^+, shows a collapse among cases after $ft \approx 20$ reaching a relatively large value of $O(6000)$, suggesting an approach to continuous turbulence. Although continuous in time, the fluctuations exhibit global intermittency. Near-wall streaks with a preferred clockwise orientation with respect to the geostrophic flow are evident. The vertical distribution of TKE shows a two-layered structure with minimum intensity at the LLJ nose height (nearly zero shear) and two maxima, one below and one above the nose. Turbulent kinetic energy near the surface is the highest in the case with the strongest stratification due to the increased shear production within the region between the surface and the LLJ nose. Such behaviour has also been reported in previous studies of the stable atmospheric boundary layer (Smedman et al. 1993; Cuxart and Jiménez 2007; Deusebio et al. 2014).

Continuous turbulence after sufficient time ($ft = 8 - 12$) is found in the present DNS of Ekman flows with stable surface buoyancy flux. The possibility that atmospheric flows have sufficient time, i.e. large enough ft, during nocturnal cooling to attain a state of continuous turbulence, even with high surface cooling flux, is larger at high latitudes with larger f.

Furthermore, the long-time stratified Ekman layer structure found here is relevant to the stable boundary layer in polar regions where winter darkness extends for weeks.

Appendix: Comparison of Constant-Temperature and Constant-Flux Stability

We have simulated two additional cases with constant-temperature stability, i.e. constant surface temperature (constant Ri_b), to illustrate their differences with the constant surface buoyancy flux cases (where Ri_b continuously changes). The time evolution of Ri_b, plotted previously in Fig. 3b, shows that the $SLD1$ case, that has an initially low value of $Ri_b \approx 0.17$, has a large value of $Ri_b = 0.62$ at $ft \approx 8$. This motivates our choice of $Ri_b = 0.62$ and $Ri_b = 0.17$ as the two constant-temperature stability cases to compare with case $SLD1$. The comparison is elaborated upon in the following paragraphs.

Profiles of mean velocity and TKE are shown in Fig. 13a, b, respectively, and compared to long-time, quasi-steady profiles of the constant Ri_b cases. The $ft \approx 8$ (when $Ri_b(t) \approx 0.62$) velocity profiles of case $SLD1$ in Fig. 13a show a stronger LLJ in the streamwise velocity component than the constant $Ri_b = 0.62$ case, and the spanwise velocity component is larger in magnitude. These differences in the mean velocity persist at a longer time of $ft \approx 30$. It is worth noting that case $SLD1$ exhibits inertial oscillations in the outer layer during its evolution unlike the cases with constant-temperature stability that achieve a quasi-steady state. At $ft \approx 8$, the $SLD1$ case is in a state just before turbulence collapse in the near-surface layer and Fig. 13b shows that the TKE is low relative to the $Ri_b = 0.62$ case. However, the TKE recovers later during the evolution of case $SLD1$ and, at $ft \approx 30$, TKE is comparable to the constant $Ri_b = 0.62$ case and slightly larger near the wall.
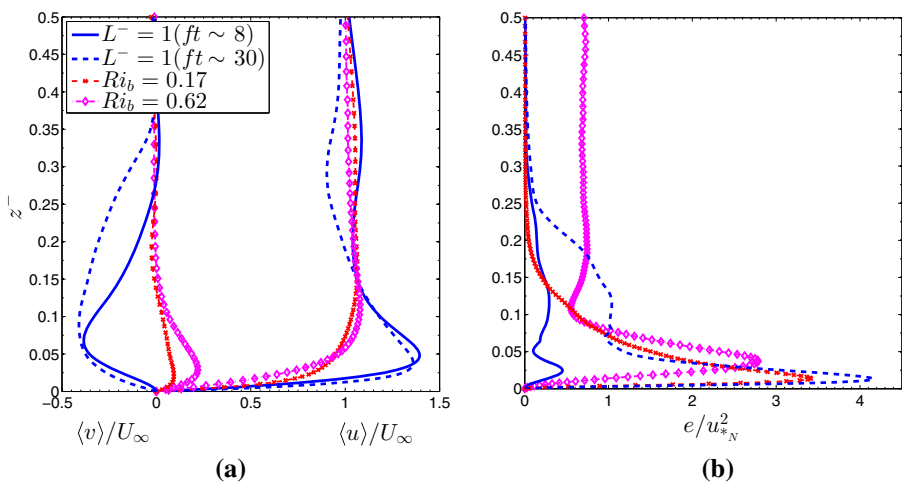

Fig. 13 Profiles of normalized statistics as a function of normalized height: **a** velocity components; (b) TKE. Here plots are presented for two cases with constant-temperature stability ($Ri_b = 0.17$ and $Ri_b = 0.62$ lines) and constant-flux stability ($L^- = 1$ lines)
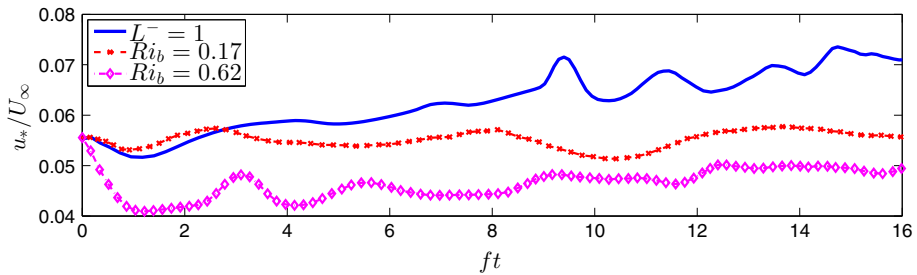
Fig. 14 The time evolution of normalized friction velocity (u_*/U_∞) for the simulated cases with constant-temperature stability ($Ri_b = 0.17$ and $Ri_b = 0.62$ lines) and constant-flux stability ($L^- = 1$ line)

Figure 14 shows differences in the time evolution of normalized friction velocity among the different cases. Case *SLD*1 has an initial $Ri_b = 0.17$ at $t = 0$ and exhibits a similar evolution of u_* as the constant $Ri_b = 0.17$ case until $ft \approx 3$. Later in time, u_* increases in case *SLD*1 to values larger than the neutral case due to the strong LLJ in the *SLD*1 case (Fig. 13a) that increases both streamwise and spanwise shear in the surface layer. The constant-temperature stability case with $Ri_b = 0.62$ shows a large initial reduction of u_* followed by an increase. However, unlike the *SLD*1 case, the value of u_* in the $Ri_b = 0.62$ case remains smaller than that in the neutral case, consistent with studies of constant-temperature stability by other investigators.

References

Ansorge C, Mellado J (2014) Global intermittency and collapsing turbulence in the stratified planetary boundary layer. Boundary-Layer Meteorol 153(1):89–116

Armenio V, Sarkar S (2002) An investigation of stably-stratified channel flow using large eddy simulation. J Fluid Mech 459:1–42

Banta R (2008) Stable-boundary-layer regimes from the perspective of the low-level jet. Acta Geophys 56(1):58–87

Banta RM, Mahrt L, Vickers D, Sun J, Balsley BB, Pichugina YL, Williams EJ (2007) The very stable boundary layer on nights with weak low-level jets. J Atmos Sci 64:3068–3090

Basu S, Porté-Agel F (2006) Large-eddy simulation of stably stratified atmospheric boundary layer turbulence: a scale-dependent dynamic modeling approach. J Atmos Sci 63:2074–2091

Beare R, Macvean M, Holtslag A, Cuxart J, Esau I, Golaz JC, Jimenez M, Khairoutdinov M, Kosovic B, Lewellen D, Lund T, Lundquist J, Mccabe A, Moene A, Noh Y, Raasch S, Sullivan P (2006) An intercomparison of large-eddy simulations of the stable boundary layer. Boundary-Layer Meteorol 118(2):247–272

Coleman G, Ferziger J, Spalart P (1990) A numerical study of the turbulent Ekman layer. J Fluid Mech 213:313–348

Coleman G, Ferziger J, Spalart P (1992) Direct simulation of the stably stratified turbulent Ekman layer. J Fluid Mech 244:677–712 (a corrigendum was published for this article in J Fluid Mech 252:721 (1993))

Conangla L, Cuxart J (2006) On the turbulence in the upper part of the low-level jet: an experimental and numerical study. Boundary-Layer Meteorol 118(2):379–400

Cuxart J, Jiménez MA (2007) Mixing processes in a nocturnal low-level jet: an LES study. J Atmos Sci 64:1666–1679

Cuxart J, Yage C, Morales G, Terradellas E, Orbe J, Calvo J, Fernndez A, Soler M, Infante C, Buenestado P, Espinalt A, Joergensen H, Rees J, Vil J, Redondo J, Cantalapiedra I, Conangla L (2000) Stable atmospheric boundary-layer experiment in Spain (SABLES 98): a report. Boundary-Layer Meteorol 96(3):337–370

de Wiel BJHV, Moene GJAF, Steeneveld P, Baas FC, A BA, Holtslag M (2012) The cessation of continuous turbulence as precursor of the very stable nocturnal boundary layer. J Atmos Sci 69:3097–3115

Deusebio E, Brethouwer G, Schlatter P, Lindborg E (2014) A numerical study of the unstratified and stratified Ekman layer. J Fluid Mech 755:672–704

Flores O, Riley J (2011) Analysis of turbulence collapse in the stably stratified surface layer using direct numerical simulation. Boundary-Layer Meteorol 139(2):241–259

Garcia-Villalba M, del Alamo JC (2011) Turbulence modification by stable stratification in channel flow. Phys Fluids 23(4):045104

Garg RP, Ferziger JH, Monismith SG, Koseff JR (2000) Stably stratified turbulent channel flows. I. Stratification regimes and turbulence suppression mechanism. Phys Fluids 12(10):2569–2594

Gayen B, Sarkar S (2011) Direct and large-eddy simulations of internal tide generation at a near-critical slope. J Fluid Mech 681:48–79

He P, Basu S (2015) Direct numerical simulation of intermittent turbulence under stably stratified conditions. Nonlinear Process Geophys Discuss 2(1):179–241

Jalali M, Rapaka NR, Sarkar S (2014) Tidal flow over topography: effect of excursion number on wave energetics and turbulence. J Fluid Mech 750:259–283

Jiménez J, Hoyas S, Simens M, Mizuno Y (2009) Comparison of turbulent boundary layers and channels from direct numerical simulation. In: Sixth international symposium on turbulence and shear flow phenomena

Jiménez MA, Cuxart J (2005) Large-eddy simulations of the stable boundary layer using the standard Kolmogorov theory: range of applicability. Boundary-Layer Meteorol 115:241–261

Katul GG, Porporato A, Shah S, Bou-Zeid E (2014) Two phenomenological constants explain similarity laws in stably stratified turbulence. Phys Rev E 89(023):007

Kosović B, Curry JA (2000) A large eddy simulation study of a quasi-steady, stably stratified atmospheric boundary layer. J Atmos Sci 57:1052–1068

Mahrt L (1999) Stratified atmospheric boundary layers. Boundary-Layer Meteorol 90(3):375–396

Marlatt S, Waggy S, Biringen S (2010) Direct numerical simulation of the turbulent Ekman layer: turbulent energy budgets. J Thermophys Heat Transf 24:544–555

Mauritsen T, Svensson G (2007) Observations of stably stratified shear-driven atmospheric turbulence at low and high Richardson numbers. J Atmos Sci 64:645–655

Monin AS (1970) The atmospheric boundary layer. Annu Rev Fluid Mech 2(1):225–250. doi:10.1146/annurev.fl.02.010170.001301

Moser RD, Kim J, Mansour NN (1999) Direct numerical simulation of turbulent channel flow up to $Re_\tau = 590$. Phys Fluids 11(4):943–945

Nieuwstadt F (2005) Direct numerical simulation of stable channel flow at large stability. Boundary-Layer Meteorol 116(2):277–299

Obukhov A (1971) Turbulence in an atmosphere with a non-uniform temperature. Boundary-Layer Meteorol 2(1):7–29

Saiki E, Moeng CH, Sullivan P (2000) Large-eddy simulation of the stably stratified planetary boundary layer. Boundary-Layer Meteorol 95(1):1–30

Shah SK, Bou-Zeid E (2014) Direct numerical simulations of turbulent Ekman layers with increasing static stability: modifications to the bulk structure and second-order statistics. J Fluid Mech 760:494–539

Smedman AS, Tjernström M, Högström U (1993) Analysis of the turbulence structure of a marine low-level jet. Boundary-Layer Meteorol 66(1–2):105–126

Spalart PR, Coleman GN, Johnstone R (2008) Direct numerical simulation of the Ekman layer: a step in Reynolds number, and cautious support for a log law with a shifted origin [Phys. Fluids 20, 101507 (2008)]. Phys Fluids 20(10):101507

Spalart PR, Coleman GN, Johnstone R (2009) Retraction: Direct numerical simulation of the Ekman layer: a step in Reynolds number, and cautious support for a log law with a shifted origin. Phys Fluids 21(10):109901

Stull R (1988) An introduction to boundary layer meteorology. Kluwer, Dordrecht, 666 pp

Sun J, Mahrt L, Banta R, Pichugina Y (2012) Turbulence regimes and turbulence intermittency in the stable boundary layer during CASES-99. J Atmos Sci 69:338–351

Tennekes H (1973) The logarithmic wind profile. J Atmos Sci 30:234–238

Zhou B, Chow FK (2011) Large-eddy simulation of the stable boundary layer with explicit filtering and reconstruction turbulence modeling. J Atmos Sci 68:2142–2155